IAEA nuclear fusion

PAPER

Survey of heating and current drive for K-DEMO

To cite this article: D.R. Mikkelsen *et al* 2018 *Nucl. Fusion* **58** 036014

IOP Publishing | International Atomic Energy Agency Nuclear Fusion

Nucl. Fusion **58** (2018) 036014 (18pp) https://doi.org/10.1088/1741-4326/aaa4d2

Survey of heating and current drive for K-DEMO

D.R. Mikkelsen[1], **C.E. Kessel**[1], **F.M. Poli**[1], **N. Bertelli**[1] **and K. Kim**[2]

[1] Princeton Plasma Physics Laboratory, PO Box 451, Princeton, NJ 08543, United States of America
[2] National Fusion Research Institute, Daejeon, 34133, Republic of Korea

E-mail: dmikkelsen@pppl.gov

Received 18 October 2017, revised 4 December 2017
Accepted for publication 3 January 2018
Published 22 January 2018

Abstract

We present calculations of heating and current drive by neutral injection and by electromagnetic waves in the ion cyclotron, helicon, lower hybrid, and electron cyclotron frequency ranges for the steady state burn conditions in a K-DEMO configuration with $I_p = 12.3$ MA, $a = 2.1$ m, $R_o = 6.8$ m, $B_o = 7.4$ T, $\bar{n}_e = 1.1 \times 10^{20}$ m^{-3}, $T(0) = 40$ keV, and $Z_{\text{eff}} = 1.5$. Lower hybrid wave current drive calculations comprise a 2D scan over poloidal launcher location and launched $n_{||}$, at a fixed frequency of 5 GHz. An ICRF frequency scan over 50–100 MHz is based on an ITER-like ICRF midplane antenna; the absorption calculation includes thermal D, T, He, Ar, and W as well as suprathermal beam ions and alphas. Helicon fast wave performance is surveyed by varying frequency over 0.6–2.5 GHz, launched $n_{||}$ from -1.6 to -3, and launcher position from top to bottom on the low-field side. An ITER-like 1 MeV neutral beam system with quasi-tangential geometry is scanned over elevation to vary the targeted minor radius. The electron cyclotron survey varies the frequency (190–300 GHz), launcher poloidal location, and the poloidal and toroidal direction of the launched waves. We report for each system the range of minor radius in which current is driven, the current drive efficiency, the optimal system parameters, and typical profiles of driven current. Electron and ion heating profiles are reported for the ICRF and NBI systems.

Keywords: K-DEMO, DEMO, current drive, heating, helicon waves

(Some figures may appear in colour only in the online journal)

1. Introduction

A conceptual design study for K-DEMO [1] was initiated in 2012, with a two-phase operational plan. The first phase is designed to demonstrate net electricity generation and a self-sustained tritium cycle, as well as provide a component test facility. After a major upgrade to replace in-vessel components, the second phase is intended to demonstrate net electric generation on the order of 500 MW. The burning plasma reference point for the K-DEMO design was selected using a systems analysis to provide the smallest facility that produces significant operating space for both phases of its mission. The systems analysis is driven primarily by the maximum achievable magnet field strength and the size determined from detailed magnet engineering, the preliminary blanket build defined by neutronics analysis, and configuration analysis.

The heating and current drive systems are critical for achieving and sustaining the plasma burn state, and for augmenting the bootstrap current to provide 100% non-inductive current in the flattop burn. The four standard types of systems have been surveyed: lower hybrid waves (LH), neutral beams (NB), ion cyclotron conventional fast waves (IC), and electron cyclotron waves (EC). All of these H/CD sources have been demonstrated on various tokamak experiments, and all, except for LH, are being developed and installed on ITER [2–4] (and a design for an ITER LH launcher has been developed [5, 6]). We have also considered current drive by helicon waves, which is being experimentally tested in current experiments [7–10] and has been proposed for reactor scale tokamaks [9, 10]. Each technology has its own set of physics and engineering advantages and disadvantages, so the final selection will depend on how well the chosen systems work together to achieve the K-DEMO design goals.

The survey calculations reported here enable the selection by providing heating and current drive profiles at plasma burn conditions. The goal of the survey is to characterize for each system the accessible range of r/a, the current drive efficiency, and the current density profiles (critically important for maintaining MHD stability). These data then enable a determination of the minimum set of systems capable of driving current everywhere it is needed across the profile, as well as the required power and other major characteristics (e.g. frequency, launcher size and location) that will determine the space requirements of each system in the vacuum vessel, the breeder blanket and the shielding. Based on systems analysis, the total power required for heating/current drive systems is expected to be in the range 80–120 MW, depending on the operating point and the selected complement of heating/current drive systems.

While the bootstrap effect provides the majority of the plasma current, external systems are required for a 'seed' current near the magnetic axis, to optimize the safety factor profile for MHD stability, and to provide a a means of actively controlling some types of instability. The auxiliary systems will be selected in order to meet these needs, and a complementary set is generally required because each system has some limitation on its applicability. IC is well suited for producing a centrally concentrated seed current, EC and NB can match a wide range of profile shapes with adequate efficiency in the warm parts of the plasma ($r/a <\sim 0.8$), while LH is well suited to driving current in the outer third of the minor radius. Helicon wave hardware would be similar to that of an LH system, but would penetrate closer to $r/a \sim 0.5$.

In tokamak reactors, only lower hybrid waves have high current drive efficiency in the outer plasma, so this is a important element in the mix of systems. We assume a passive-active multi-junction (PAM) waveguide [5, 6] is the launching structure, and locate it on the low field side. Although there is some motivation for launching from the high field side [11, 12] this is not a demonstrated approach.

Heating and current drive by electromagnetic waves in the ion-cyclotron range of frequencies (ICRF) is well developed theoretically, and is well suited for current drive near the magnetic axis. The high temperatures required for burning plasmas guarantee strong single-pass damping for electrons, majority ion species and unthermalized fusion-product alpha particles. Current drive is optimized by minimizing damping by any ion species, so the frequency should be just below $2\Omega_{\mathrm{cD}}$ at the outboard edge of the plasma (with the $2\Omega_{\mathrm{cT}}$ resonance at $R < R_{\mathrm{axis}}$) and the parallel wavenumber should be chosen to minimize damping by alphas [13, 14]. Accordingly, we have considered only a midplane launcher, because alpha damping cannot be strictly minimized with off-midplane launchers: it is more difficult to launch a pure $k_{\|}$ spectrum [15], and the opposing requirements on $k_{\|}$ to both enhance electron absorption and minimize fast alpha absorption produce higher alpha absorption than for a midplane launcher [16]. Although the studies of ICRF current drive cited above were limited to a few EU DEMO designs, their qualitative guidance for midplane launchers has been validated by both the (advanced) ACT1 [17] and (conservative) ACT2 [18] design studies.

Current drive by helicon waves (fast waves with ω greater than $\sim 20\Omega_{\mathrm{ci}}$) is attractive in calculations for tokamak reactors [9, 19–21], but early experiments were puzzling [22]. More recently, however, combline traveling wave antennas designed for fast wave current drive have been successfully tested on DIII-D [23], JFT-2M [7] and KSTAR [8, 24], and new current drive experiments are planned on DIII-D [9] and KSTAR [25]. There is no published guidance from comprehensive surveys, so we have varied the frequency, the launcher position, and the launched $n_{\|}$ to establish the range of possible current drive performance.

Neutral beam injection has been extensively studied in tokamak experiments and for tokamak reactors. The required particle energy, ~ 1 MeV, and the need for quasi-tangential geometry are well established. We have explored a novel means of tailoring the current drive profile at intermediate minor radii, $0.2 < r/a < 0.7$, by using beam paths out of the midplane but parallel to it.

Current drive by electron cyclotron waves [26] is potentially useful for active control of MHD instabilities [27–30], and also can provide current drive in the intermediate region of the plasma for fine-tuning the safety factor profile. EC current drive has been studied extensively for ITER [4, 29, 31–34], and DEMO configurations [35]. In high temperature plasmas ($T_{\mathrm{e}0} \geqslant 30$ keV) it is important to minimize second harmonic absorption [32, 36, 37] by limiting the frequency or using off-midplane launchers [32, 38]. System optimization should include poloidal [33] and toroidal steering, so we have scanned over both, as well as varying the launcher location and frequency.

The plasma and tokamak configuration parameters used for our heating and current drive calculations are described in section 2. The expected heating and current drive is characterized separately for each method: lower hybrid waves in section 3, ion cyclotron waves in section 4, helicon waves in section 5, neutral beam injection in section 6, and electron cyclotron waves in section 7. Simulation methods, inputs, and resolution choices are discussed within each of these sections. The results are summarized in section 8.

2. K-DEMO burning plasma conditions

The K-DEMO reference point was selected [39] using a systems analysis code [40], based on the maximum achievable magnet field strength and the size determined from detailed magnet engineering, the preliminary blanket build by neutronics analysis, and configuration analysis. The operating point's macroscopic characteristics are $I_{\mathrm{p}} = 12.3$ MA, $B_{\mathrm{o}} = 7.4$ T, $a = 2.1$ m, $R_{\mathrm{o}} = 6.8$ m, $\kappa = 2.0$, $\delta = 0.625$, $q_{95} = 7$, $\bar{n}_{\mathrm{e}} = 1.4 \times 10^{20}$ m^{-3}, $Z_{\mathrm{eff}} = 2$, and a bootstrap fraction of 0.7–0.8.

The burning plasma conditions are further refined with the Tokamak Simulation Code [41] (TSC), a predictive plasma evolution code, solving the free-boundary 2D axisymmetric MHD Maxwell's equations on a rectangular (R,Z) grid. The surface-averaged transport equations are solved to obtain the temperature profiles, utilizing a modified Coppi–Tang

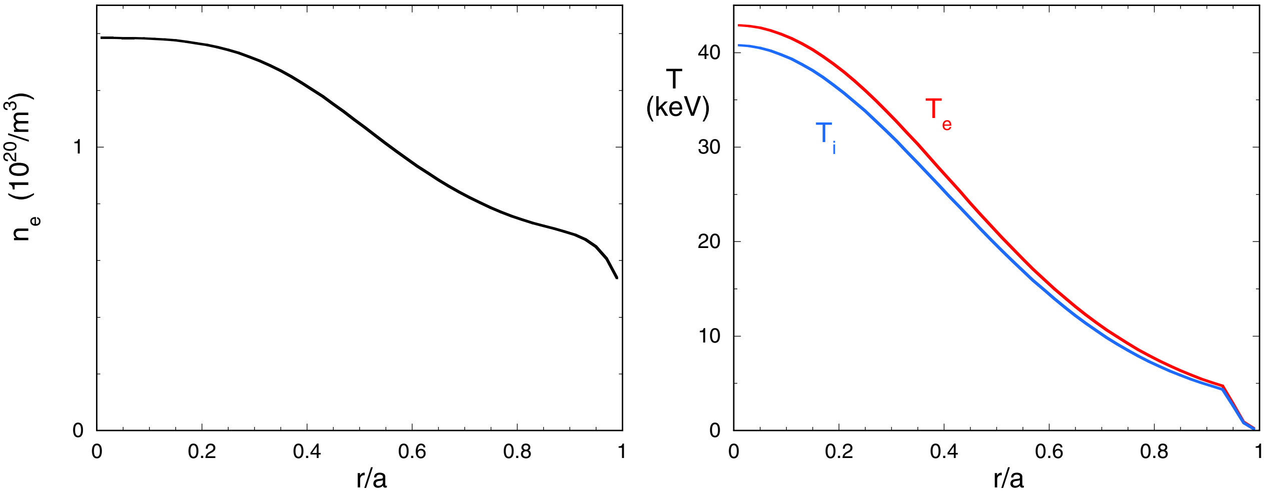

Figure 1. The plasma profiles used in the heating and current drive calculations: electron density, electron and ion temperatures.

[42, 43] transport model with a prescribed temperature pedestal. Density peaking is predicted [44, 45] for burning plasmas in ITER ($n_e(0)/\langle n_e\rangle \sim 1.5$), so the density profile is prescribed with a peak to volume average of 1.4–1.5, an edge pedestal and finite separatrix density at 0.35 times the central value, n(0), see figure 1; the radial variable is defined as $r/a = \sqrt{\Phi_{\rm tor}/\Phi_{\rm N}}$, the square root of the edge normalized toroidal flux.

The code is used to develop a time-dependent scenario to determine the plasma temperatures, the individual coil currents, the plasma shape as it grows, and the heating and current drive evolution. The simulation begins early in startup ($I_p = 500$ kA) and runs long enough for current density profiles be close to steady state. The initial plasma width is the same as in the burning phase, limited on the inboard wall, and the plasma boundary grows (primarily vertically) to it's full size and shape over the course of 30 s, the H-mode phase begins at 75 s, and the current-ramp extends to 120 s. The plasma magnetic divertor X-point forms very early in order to isolate the plasma from the wall and allow the injection of heating and current drive power.

The thermal diffusivity is adjusted as the run proceeds to provide sufficient global confinement to reach the desired β level, as identified by the systems analysis. For the burning plasma phase the temperature at the top of the pedestal was assumed to be 4.5 keV, although the pressure limit at the top of the pedestal as determined by a correlation based on peeling ballooning model EPED1 [46] for ITER, predicts Tped 5–5.5 keV. In order to raise the radiated power to a significant level argon and tungsten are included at 0.1% and 0.001%, respectively, of the electron density. The alpha and auxiliary heating is primarily delivered to the electrons, but the ion temperature is collisionally coupled to the electron temperature across the entire profile (figure 1).

Most of the heating and current drive calculations described in sections 3–7 are based on the magnetic equilibrium and plasma profiles taken from the stationary, full power, burning plasma phase of the TSC discharge scenario. Additional calculations with temperatures scaled down provide a guide to the sensitivity of the results, and the current drive achievable during earlier phases of operation.

The computational procedures used in this work were originally developed for the (advanced) ACT1 [17] and (conservative) ACT2 [18] tokamak reactor design studies. Those publications provide additional detail on the methods and simulation results for somewhat different configurations.

3. Lower hybrid wave heating and current drive

Lower Hybrid waves are considered as a current drive tool for the K-DEMO device [47, 48]. These waves typically drive current in the outer 1/3 of the plasma minor radius. The LH assessment done here assumes it is launched from the low field side, although there are interesting results for launching from the high field side [12]. The launching structure is envisioned to be the passive-active multi-junction (PAM) waveguide [5, 6].

The frequency, 5 GHz, is chosen to balance the minimization of LH power absorbed on fast alpha particles [49–52] against the need to keep the waveguide width sufficiently large so it can be manufactured [53]. The K-DEMO conditions require only modest extrapolation from the multi-parameter survey calculations of alpha particle absorption in [52]. where the alpha absorption is found to be 1.1% at 5 GHz, $T_e = 20$ keV, $B_o = 6$ T, $n_\parallel = 2.0$, and $n_e = 8 \times 10^{19}$ m^{-3}. The density dependence is negligible, $n_\parallel = 2$ is a good choice for K-DEMO, increasing B_o to 7.5 T should increase the absorption by ~20%, while increasing T_e to 40 keV should increase absorption by ~50%, so the extrapolated alpha absorption is estimated to be 2% for K-DEMO. The absorption rises rapidly as the frequency is reduced [52] (by a factor of seven at 3.7 GHz), so we have adopted a single frequency for this study.

The Lower Hybrid Simulation Code (LSC) [54], a 1D ($v_\parallel$) Fokker–Planck treatment with ray tracing, is used to determine the wave propagation, damping, and current drive produced by lower hybrid waves. The launched spectrum is modeled as two Gaussian lobes, one in the co-I_p direction with $n_\parallel$ varied in the calculations, and the other in the counter-I_p direction with fixed $n_\parallel = -4.0$. Each lobe has a FWHM $\Delta n_\parallel = 0.2$, chosen to broaden the distribution of

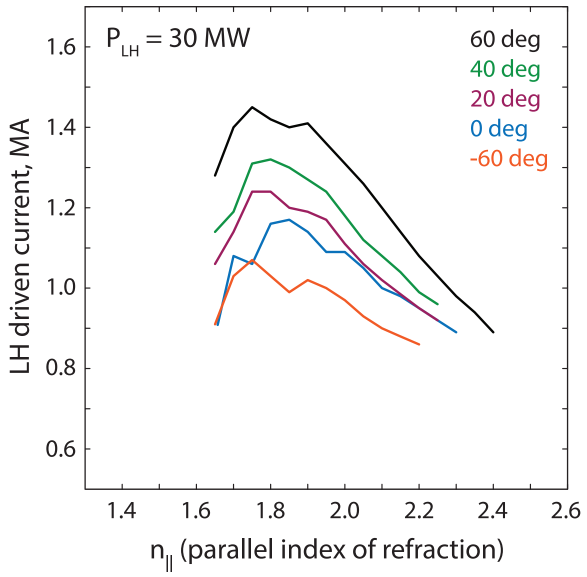

Figure 2. Total current driven by 30 MW of injected lower hybrid waves as a function of the $n_{||}$ of the co-I_p lobe, for launchers at a range of poloidal angles.

driven current and avoid a narrow profile with a very high peak current density. More detailed descriptions of the spectrum will need to await design of the launching structure. The power fraction distribution typical of PAM launchers is 70–75% in the co-I_p and 25–30% in the counter-I_p directions. Here we model the power split as 83% in the co-I_p and 13% in the counter-I_p lobes in order to match the total driven current calculated with a more accurate 2D Fokker–Planck treatment in GENRAY/CQL3D [37, 55, 56].

Shown in figure 2 is the total driven LH current for 30 MW of injected power as a function of $n_{||}$ of the co-I_p lobe, for different launcher positions, labeled by the launcher's poloidal angle on the outboard side. Increasing the launcher's poloidal angle improves the current drive efficiency, and generally leads to deposition at lower minor radii. The accessibility condition [48] for LH waves leads to a variation in the driven current and the deposition location as $n_{||}$ is varied. At low values the slow waves are cutoff and are converted to fast waves, which propagate back to the plasma boundary, reflect, and damp at larger minor radii. At high values the expression for maximum electron Landau damping [57] leads to damping at larger minor radius. Figure 3 shows three driven current profiles for waves launched from the outboard side at 40° above the midplane, and with $n_{||} = 1.65$, 1.90, and 2.20. The low $n_{||}$ case shows current driven around $r/a = 0.9$, which is fast wave driven current, and current driven over $r/a = 0.65{-}0.9$ driven by slow waves, for a total of 1.14 MA. The middle value shows driven current centered at $r/a = 0.78$, but distributed from 0.68 to 0.95, all driven by slow waves, for a total of 1.26 MA. The high value has a current driven from 0.78–0.95, all driven by slow waves, for a total of 0.99 MA. All cases have the negative driven current associated with the counter-I_p lobe of the launched spectrum. The LH penetration into the plasma has benefited from the high toroidal field used in the K-DEMO design, which improves the accessibility condition.

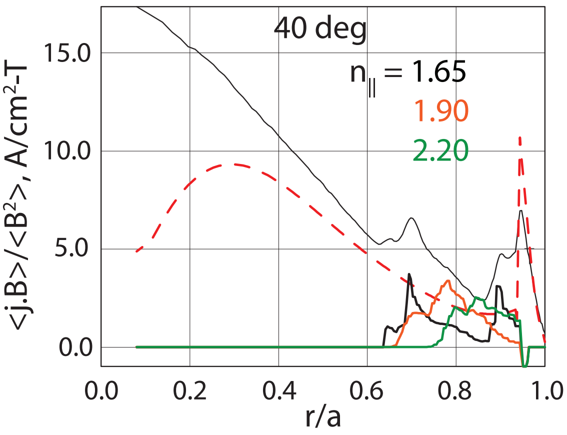

Figure 3. Current drive profiles for lower hybrid waves launched from the outboard side at 40° above the midplane, at three $n_{||}$. The thin black line peaked at the center is the total parallel current, and the dashed red line represents the bootstrap current.

4. Ion cyclotron wave heating and current drive

Electromagnetic waves in the ion cyclotron range of frequencies, or ICRF, can be used to heat ions and electrons and, when phased appropriately, will also drive current near the magnetic axis, typically for $r/a \leqslant 0.3$. This current drive function is very important for providing a seed current that avoids high values of the on-axis safety factor. Finding the ICRF system parameters that maximize the current drive efficiency is the focus of our study, and this requires maximizing both the wave damping on electrons and the asymmetry in their velocity space distribution that is responsible for generating a net current.

The ion cyclotron range of frequencies is quite broad, but experiments and design studies are typically limited to the fundamental through second harmonic of the ion cyclotron frequencies. As a consequence of the $1/R$ variation in the toroidal magnetic field strength, some frequencies match the fundamental cyclotron resonance and second harmonic of several ion species at different locations within the plasma (see figure 4). In order to quantitatively assess the relative importance of the competing channels for wave damping, the ACT1 [17] and ACT2 [18] power plant studies found that it is important to include resonances with all the ion species, so our calculations include thermal populations of deuterium, tritium, helium ash, argon, tungsten, and suprathermal fusion-produced alphas and neutral beam injected deuterium.

TRANSP [58, 59], is used to calculate heating and current drive produced by ICRF fast-waves. The TRANSP simulations are based on TSC's magnetic equilibrium and its profiles of electron and ion density and temperature.

The TORIC [60, 61] full-wave code (installed in TRANSP) is used for conventional fast-wave ion cyclotron waves. These calculations include a Fokker–Planck treatment of the resonant ions, while using an equivalent Maxwellian distribution for the suprathermal alphas and neutral beam injected deuterons. The use of slowing down distributions is more accurate, but Maxwellians provide qualitatively correct results

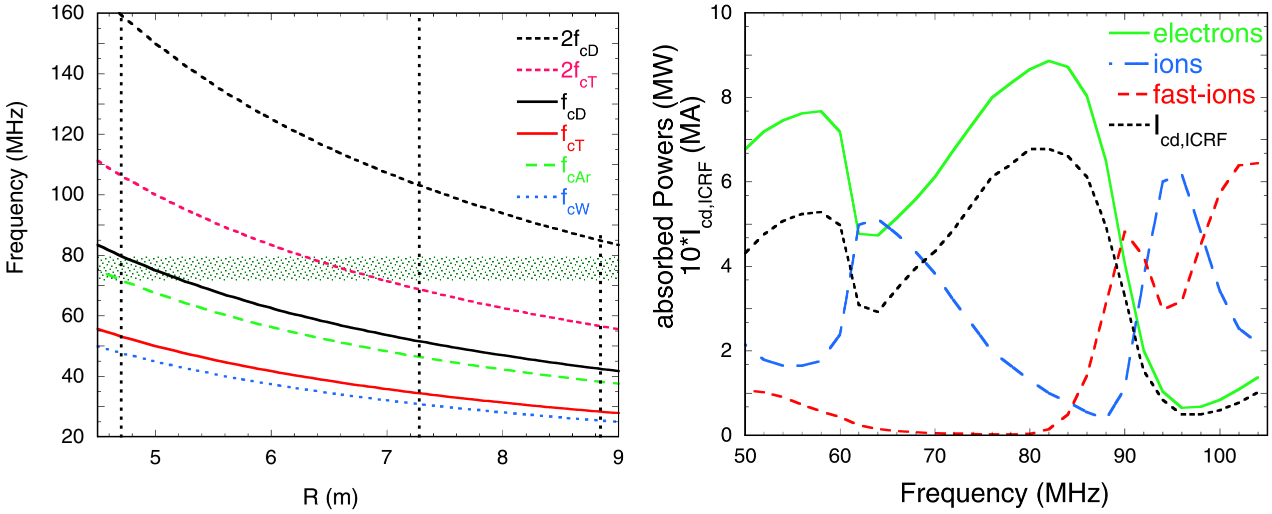

Figure 4. Left: ion cyclotron 'cold resonance' frequencies versus major radius for several ion species. The vertical dashed lines designate the locations of the inner and outer limits of the plasma as well as the magnetic axis. The shaded horizontal band indicates the most favorable frequency band for current drive and minimizing absorption by alpha particles. Right: ion cyclotron driven current (times 10, in MA) and power absorbed by electrons, all thermal ions, and all suprathermal ions versus frequency; for 10 MW launched.

[15, 62], which is a sufficient guide for avoiding strong absorption on suprathermal populations.

The driven current is calculated using the Ehst-Karney non-relativistic, asymptotic formula [63], which includes toroidal trapping effects. Comparisons with Fokker–Planck treatments of the electron distribution support the use of the analytic approximation even when $\omega/k_{\|} \sim v_{\mathrm{th,e}}$ [64, 65] . Relativistic corrections are not expected to be large, even though $T_{\mathrm{e}} \sim 40$ keV, because $|n_{\|}| = ck_{\|}/\omega \sim cn_{\mathrm{tor}}/(\omega R_{\mathrm{axis}}) \sim 3$ for the optimal conditions.

The antenna characteristics are based on the ITER multi-strap launcher design [3], which has a maximum power density through the first wall of 10 MW/m2. With the antenna placed at the outboard midplane of K-DEMO, the toroidal mode number is 30. To determine the sensitivity of the results to possible modifications of the antenna, additional full frequency scans were carried out with the toroidal mode number set to 23 and 37, but the results were very similar to those shown in section 4.

Figure 4 provides an overview of the heating powers (to electrons, all thermal ions, and all suprathermal ions) and the current driven by 10 MW, for frequencies from 50 to 110 MHz. The driven current closely follows the power coupled to the electrons, which would be high at all frequencies (for these temperatures) but for the strong ion resonances that damp the waves before they can reach the hot electrons near the magnetic axis.

Below 60 MHz the ion coupling occurs at the fundamental resonances with thermal and suprathermal deuterium and alpha particles that are located at small major radius ($R < R_{\mathrm{axis}}$), so only a little power is coupled to ions. The second harmonic of tritium at the outboard edge of the plasma lies at 58 MHz, and as the frequency is raised above this the ion absorption grows rapidly because the $2\Omega_{\mathrm{cT}}$ resonance location moves into hotter plasma, peaking when the resonance major radius is still outside the magnetic axis. At still higher frequencies the electrons near the axis absorb a rising fraction of power before the waves can reach the $2\Omega_{\mathrm{cT}}$ resonance which is then located at increasingly smaller $R < R_{\mathrm{axis}}$.

Above 80 MHz the ion heating rises and falls again as the $2\Omega_{\mathrm{ci}}$ resonances for deuterium and alphas enter the plasma, move toward the magnetic axis and beyond it. Note that the second harmonic absorption by unthermalized deuterium and alpha particles also becomes very large, and this is quite broad in frequency because their broad velocity distribution can produce Doppler matching of the resonance for a larger range of frequencies. The relatively small fast ion absorption below 70 MHz occurs at the fundamental resonance, which is located in the unfavorable region $R < R_{\mathrm{axis}}$.

The current drive efficiency has two maxima, at frequencies that minimize the ion coupling because the D and T $2\Omega_{\mathrm{ci}}$ resonances are at the outboard edge of the plasma and the fundamental resonances are at $R < R_{\mathrm{axis}}$. Aside from the slightly lower current drive efficiency, the lower frequency band less favored because it has much higher absorption on suprathermal alphas that would generate trapped-particle orbit loss, and insertion of helium into the first wall materials.

The fast-ion acceleration and loss (mainly of alpha particles) can best be minimized in the range 74–80 MHz, where the current drive efficiency, 60–70 A kW^{-1}, is near its maximum. This range is also advantageous in the early phase of the discharge when it matches the $2\Omega_{\mathrm{cT}}$ resonance near the magnetic axis, enabling efficient ion heating when low electron temperature limits the electron absorption.

The optimal ICRF frequency is therefore slightly below 80 MHz, where coupling to suprathermal alphas is minimized and current drive is near its maximum efficiency. This conclusion is robust against changes in the toroidal wave number (varied from 23 to 37), and is also unchanged if there is no neutral beam injection or the neutral beam injected fast deuterium population is moved radially because the suprathermal alphas dominate the fast particle absorption in all these scenarios. The precise value of expected damping on suprathermal alphas requires use of a non-Maxwellian distribution

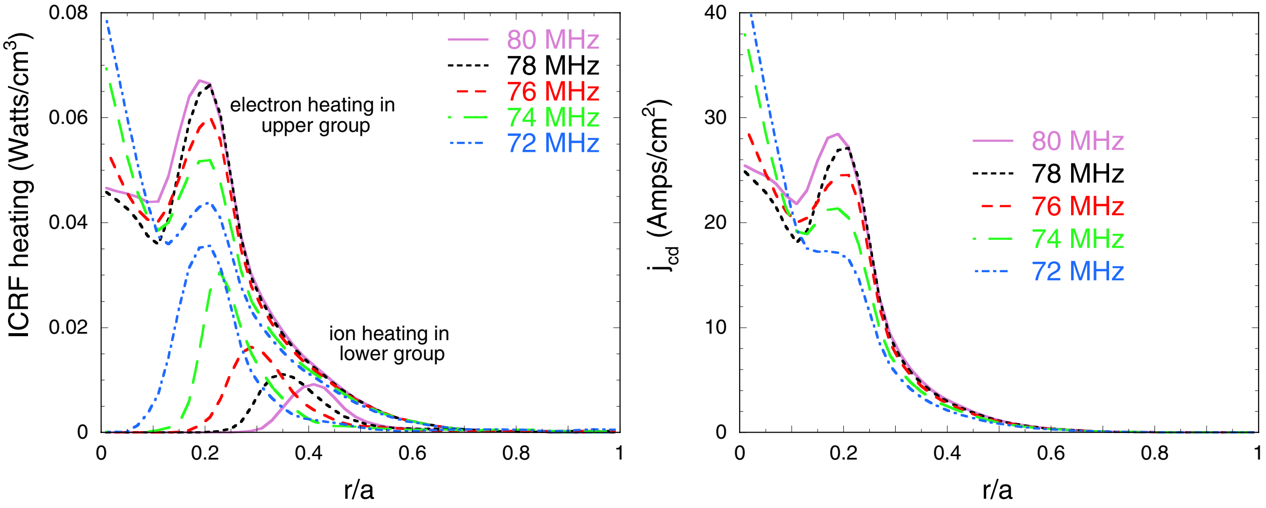

Figure 5. Ion cyclotron heating and current drive profiles versus minor radius in the most favorable frequency range.

function [62], but alpha damping is expected to be minimized in or near the frequency range identified here.

The heating and driven current profiles for the relatively narrow optimal frequency range, shown in figure 5, reveal a large change in the ion heating magnitude and its radial location. Both changes are caused by the varying location of the $2\Omega_{cT}$ resonance as it moves to increasingly lower $R < R_{axis}$ as the frequency approaches 80 MHz. Resonances with other ions absorb little power in this frequency range. The electron absorption is stronger for higher electron temperature, so it and the driven current are concentrated near the magnetic axis. The relatively small changes in electron heating and current drive profiles are indirectly caused by the changes in the tritium absorption.

5. Helicon wave heating and current drive

Helicon waves launched from the outboard side of the plasma are examined as a means to provide current drive for fine-tuning the safety factor profile in the region of the plasma with $0.2 < r/a < 0.6$. With outboard launchers, neither conventional ICRF fast waves nor lower hybrid waves can drive current in this radial range, but neutral beam injection and electron cyclotron waves are capable of localized current drive with width $\Delta r/a \sim 0.25$.

In this frequency range wave absorption by suprathermal fusion product alpha particles and neutral beam ions can be very significant [9, 19–21]. The calculations reported here include both populations, as well as thermal electrons, deuterium and tritium. In all cases the coupling to unthermalized beam ions is smaller than the alpha coupling. The strongest motivation for minimizing wave coupling to alphas is to minimize implantation of energetic alphas in the surrounding structure. In the results presented below we have required that the power coupled to alphas be not more than 1% but, as discussed below, the results are little changed if the limit is smaller or larger by a factor of five because the current drive is tied to electron absorption, which remains high even with 5% alpha absorption. In the region of parameter space where alpha coupling transitions from small to significant, the alpha absorption depends strongly on $n_{\|}$ and the launcher location, so optimal values for both parameters are nearly unchanged when the allowed alpha absorption is varied but still required to be small. Qualitatively different results for current drive efficiency and for the optimal parameters are possible with significant alpha absorption (i.e. $\geqslant$30%) but this is considered unacceptable for power plant operation and such cases not discussed below.

The density and temperature ($\equiv (2/3)\langle E\rangle$, $\sim$1 MeV for the alphas, $\sim$300 keV for the deuterium fast ions) are taken from the standard TRANSP simulation of K-DEMO. Maxwellian distributions have been assumed for the thermalizing fast ions so the accuracy is not high [15, 62], but, for the reasons discussed above, the current drive efficiency and optimal launcher parameters reported here are expected to be close to what would be obtained from calculations employing slowing down distributions.

For this study the GENRAY ray-tracing code [37, 55] was used to calculate ray propagation, wave absorption and current drive. Benchmark calculations [66, 67] with the AORSA full-wave code [68] have confirmed the expectation that GENRAY is capable of sufficient accuracy for this task. Absorption is calculated using the fast wave model of Chiu, *et al* [19]. Previous work [9, 21] has found that high power helicon waves do not create serious quasilinear distortions of the electron distribution function, so the electron velocity-space distribution is assumed to be Maxwellian here. The driven current is calculated from the Ehst-Karney non-relativistic, asymptotic formula [63], which includes toroidal trapping effects. Relativistic corrections are not expected to be large, even though $T_e \sim 40$ keV, when $|n_{\|}| = ck_{\|}/\omega \geqslant 2$, but the highest current drive efficiencies were obtained with launched $|n_{\|}| = 1.6$ so these must be considered provisional (at the half-power point along the ray path $|n_{\|}|$ has grown to 1.8). In any case, the efficiencies for launched $|n_{\|}| = 2$ are almost as high.

The optimal conditions for launching helicon waves and coupling to the electrons to maximize current drive are

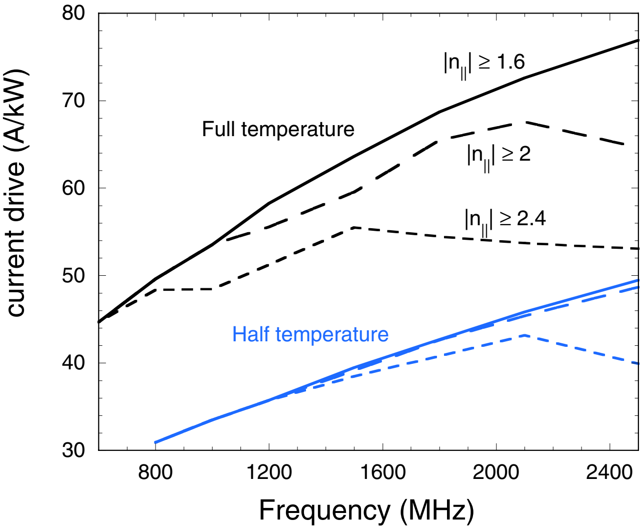

Figure 6. Maximum helicon wave current drive efficiency versus frequency, for three lower limits on $|n_{||}|$ and two temperature profiles. The solid lines allow $|n_{||}|$ as low as 1.6, the long-dashed lines are achievable with $|n_{||}| \geqslant 2.0$, and the short dashed lines are for $|n_{||}| \geqslant 2.4$. The lower group of lines is for the reduced temperature calculations.

complex, and not easily summarized. Early experiments may have suffered from strong coupling to slow waves in the scrape-off layer near the antenna [22] as may be occurring in more recent high harmonic fast wave experiments [69, 70] and this possibility may arise with reactor-grade plasmas as well [67]. In this study we did not have the resources to address this complicated issue, but recent work at KSTAR [24] suggests that this problem can be managed. Detailed discussions of this topic are found in [9, 20, 21, 24]. In this work we have assumed there are no losses in the SOL: that all of the launched power propagates as a fast wave to the ray tracing initial location, just inside the last closed flux surface.

Finding the optimal parameters of the helicon wave system requires a three dimensional parameter scan varying the wave frequency, launcher position, and $n_{||}$ at the launcher. In the work presented here, the frequency was varied from 0.6 to 2.5 GHz, while the launcher position ranged from directly below the magnetic axis to directly above the axis. The value of $n_{||}$ at the launcher will be determined by the characteristics of the launcher, so it is a free parameter at this stage of the design. We have spanned $-3 \leqslant n_{||} \leqslant -1.6$, which covers the typical values used in previous work on helicon waves.

Survey calculations were carried out with the single-ray model in GENRAY. The results exhibit weak dependence on the launcher position and on $n_{||}$ (near the optimal values of these parameters), so there is no reason to expect that multi-ray representations of the waves will produce significantly different results for either the current drive efficiency or the radial profile of the driven current.

5.1. Helicon wave current drive efficiency

For an overview of the results (figure 6) we present the highest current drive efficiency obtained for each frequency, selected from a two dimensional scan over launch position and $n_{||}$, after excluding all cases with more than 1% of the power coupled to alpha particles. It is presently unclear what the practical lower limit on $|n_{||}|$ at the launcher will be, so the results are reported for three lower limits: 1.6, 2.0, and 2.4.

The highest current drive efficiency is obtained with highest frequency and the lowest $|n_{||}|$ in the scan: 1.6. It is not presently clear whether suitable launchers for this value are realizable [9, 21] while avoiding coupling to slow waves [24], so larger values for the lower limit on $|n_{||}|$ should also be considered. However, at the lower frequencies we find that a larger $n_{||}$ is required in any case to reduce the alpha coupling to an acceptable level. If $|n_{||}|$ must be at least 2 at all frequencies, the maximum current drive efficiency is reduced a bit and the frequency dependence is nearly flat above 1.8 GHz. These trends are more pronounced if we require that $|n_{||}| \geqslant 2.4$, with a substantial reduction in peak current drive efficiency, but only a ±10% variation across the full frequency range studied here. Even the lowest efficiencies in figure 6 are comparable to the current drive efficiency for neutral beams and electron cyclotron waves, the other technologies that can drive current at intermediate radii.

When the electron and bulk ion temperatures are lowered by 50% there is a significant reduction in current drive efficiency. For low limits on $|n_{||}|$ the efficiency scales roughly $\propto T_e^{0.6}$. With the lower temperatures we find that the efficiency depends weakly on the lower limit for $|n_{||}|$, except at the highest frequency. The lack of variation at lower frequencies occurs because low values of $n_{||}$ are excluded from consideration by their large alpha damping. For 1.2 GHz there were no $n_{||}$ (in the range studied) with sufficiently low alpha damping, so this frequency is missing from the left plot of figure 7.

5.2. Optimal poloidal location for helicon wave launchers

The current drive efficiency depends weakly on the poloidal location of the launcher, as shown in figures 7 and 8. For $|n_{||}| = 1.6$ and 2.0, (figure 7) the efficiency rises as the launcher is moved toward the bottom of the plasma. The results from all the frequencies studied here are qualitatively the same, although the range of Z_{launch} that is consistent with low alpha absorption is quite narrow for frequencies ⩽1 GHz.

For the two lowest limits on $|n_{||}|$, the optimal launcher location is set by our limit on the power absorbed by fusion product alpha particles because the alpha coupling rises steeply as the launcher position is lowered. While our assumption of a Maxwellian alpha energy distribution reduces the accuracy of the estimated coupling, the steepness of the rise shows that even errors of +100% can be accommodated by moving the launcher location up by 10–20 cm; this will lead to very little change in the current drive profile or efficiency.

For frequencies near or below 1 GHz, there is only a narrow range of locations (near the top of the plasma) with very small alpha absorption, and below 1 GHz it is necessary to require $|n_{||}| \geqslant 2.4$ as well. This is consistent with previous reactor studies [19, 20] that found very significant alpha absorption for frequencies at the low end of the 'helicon'

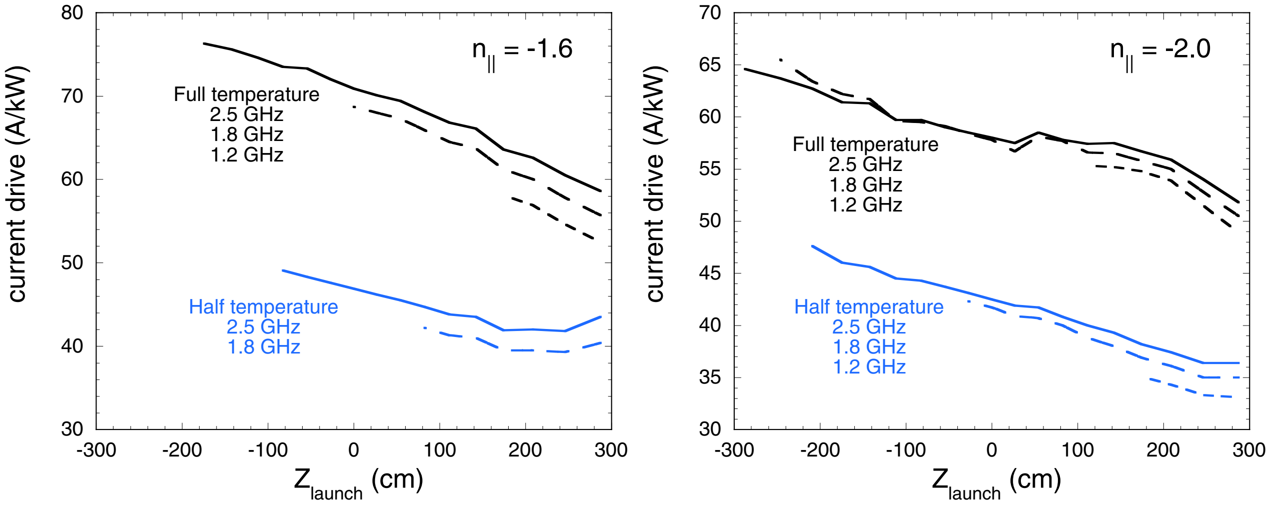

Figure 7. For $n_{\|} = -1.6$ (left) or -2.0 (right), the maximum helicon wave current drive efficiency versus $Z_{\rm launch}$, for three frequencies and two temperature profiles. The solid lines are for 2.5 GHz, the long-dashed lines for 1.8 GHz, and the short dashed lines are for 1.2 GHz. The lower group of lines is for the reduced temperature calculations.

range ($\sim 20\Omega_{\rm ci}$) and below that in the 'high-harmonic fast-wave' (HHFW) range [71, 72]

For $n_{\|} = -2.4$ the dependence on launcher location changes qualitatively (figure 8) when the burning plasma temperatures are used. The current drive efficiency no longer falls as the launcher is raised above the midplane; instead it rises to a level that is only ~10% below the maximum achieved with the launcher near the bottom of the plasma. In these conditions the minimum efficiency occurs at the midplane, about ~25% below the maximum efficiency. With the reduced temperature profile, however, the location dependence is similar to that with the smaller $|n_{\|}|$ in figure 7.

5.3. Helicon wave current drive profiles

Helicon wave current drive is quite localized (figure 9), only electron cyclotron waves can produce a narrower current channel. The width of the current profile is slightly broader with larger $|n_{\|}|$ at the launcher or with lower frequencies; the full width at half maximum (FWHM) is shown in figure 10. For a given magnetic geometry and set of temperature profiles, the location of the current drive *for cases with very low alpha coupling* is essentially independent of frequency, launcher location, and launched $n_{\|}$. Lower temperature reduces the dominant coupling to electrons, so the waves are not fully absorbed until they are closer to the magnetic axis in this case.

With frequencies in the range of 0.5–0.7 GHz it is possible to drive current close to the axis, but the estimated alpha absorption in such cases is tens of percent, as reported previously for significant current drive near the magnetic axis [20, 21]. If the alpha absorption is limited to $\leqslant$1–5% there is no set of parameter choices that will generate significant helicon current drive for $r/a \leqslant 0.4$ in the burning plasma conditions. The inability of these parameters to affect the current drive location is the greatest limitation of helicon wave current drive.

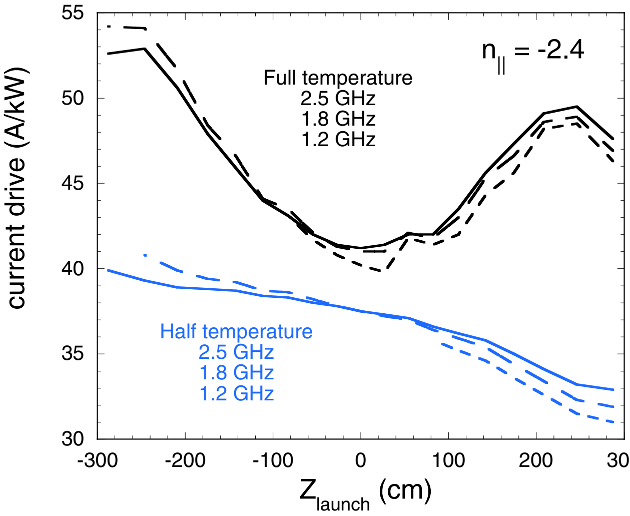

Figure 8. For $n_{\|} = -2.4$, the maximum helicon wave current drive efficiency versus $Z_{\rm launch}$, for three frequencies and two temperature profiles. The solid lines are for 2.5 GHz, the long-dashed lines for 1.8 GHz, and the short dashed lines are for 1.2 GHz. The lower group of lines is for the reduced temperature calculations.

6. Neutral beam injection heating and current drive

Negative-ion neutral beams could provide efficient current drive with a wide variety of profile shapes in the gap between central deposition of ICRH and the peripheral absorption of lower hybrid waves. This flexibility is needed in order to produce a safety factor profile that will allow maximum plasma pressure while maintaining MHD stability.

The NUBEAM [73] Monte Carlo orbit following package in TRANSP was used to calculate the neutral beam deposition, collisional thermalization, bulk heating and current drive. We consider orientations with tangency radii of 4.95–5.2 m (rising with elevation, $|Z|$, see figure 11), and the parameters of the ITER 1 MeV neutral beam design [2] are adopted. The

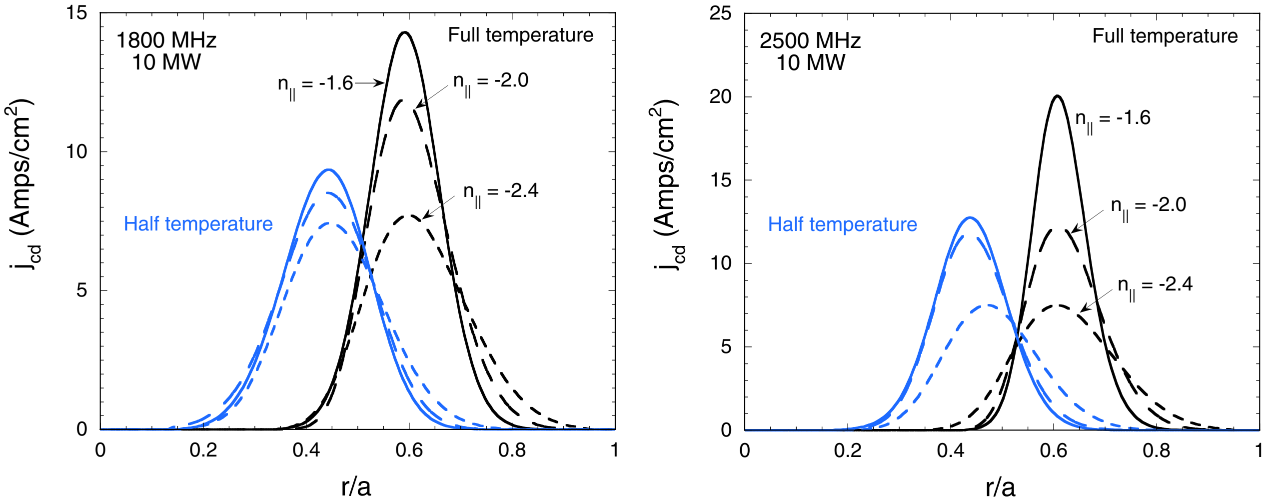

Figure 9. For 1.8 GHz (left) and 2.5 GHz (right), the radial profiles of driven current for the optimal cases with three lower limits on $|n_{||}|$ and two temperature profiles. The solid lines represent $n_{||} = -1.6$, the long-dashed lines are for $n_{||} = -2.0$, and the short dashed lines are for $n_{||} = -2.4$. The group of curves on the left is for the reduced temperature calculations.

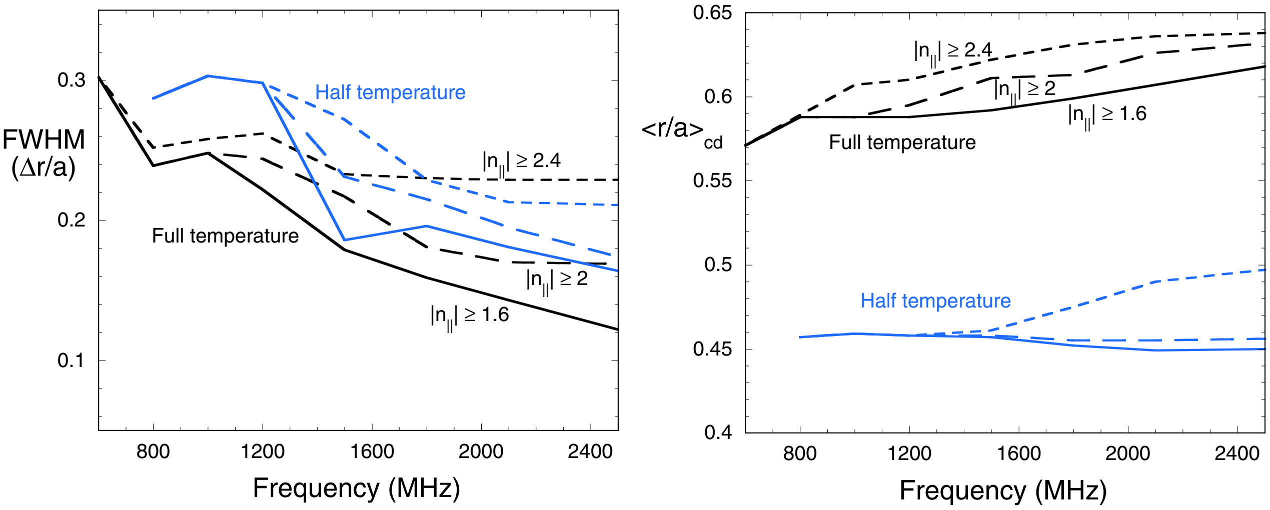

Figure 10. Frequency dependence of current drive profile full-width at half-maximum (left) and average radius (right) for the optimal cases with three lower limits on $|n_{||}|$ and two temperature profiles. The blue group of lines is for the reduced temperature calculations.

rectangular ion source is 0.28 m wide and 0.76 m tall, the rectangular beam port at the tokamak is 0.29 m wide and 0.61 m tall. The neutral paths emitted from different parts of the source tend to converge toward a focal point in the center of the port, and then diverge as they travel beyond the focal point to the point of minimum r/a, roughly at $R = R_{\mathrm{axis}}$. The source to port distance is 23.3 m, so the defocused 'image' of the source is only a few cm across, and the neutral beam footprint at $R \sim R_{\mathrm{axis}}$ is dominated by the 0.005 radian divergence caused by the finite ion temperature in the ion source. The $1/e$ half-width of the beam footprint is ~0.2 m. Near the magnetic axis the calculation typically exhibits some Monte Carlo 'noise' caused by the relatively small number of sample particles that contribute to the small near-axis zones. This noise has been reduced by using 16 000 sample particles, non-uniform weighting (WGHTA = 20.0) and time averaging over 16 s for each beam orientation.

6.1. Neutral beam injection geometry

The plasma minor radius is much larger than the diameter of the neutral beam footprint, so the deposition profile could be quite locally concentrated if all parts of the ion source are aimed on the same spot. Alternatively, by suitably aiming different sub-regions of the ion accelerator [74] it should be possible to match a desired heating or current drive profile of any shape likely to be needed in the plasma core ($r/a < 0.8$). A tall, narrow port is needed for full profile flexibility, but the impact on tritium breeding of such a gap in the blanket would need to be assessed. The results presented here illustrate the minimum radial broadening produced by the expected beam divergence; actual operation would typically require a broader radial distribution that would be achieved by adjusting the beam aiming.

The neutral beam path must be straight and it must be threaded between TF coils, blanket modules, and other

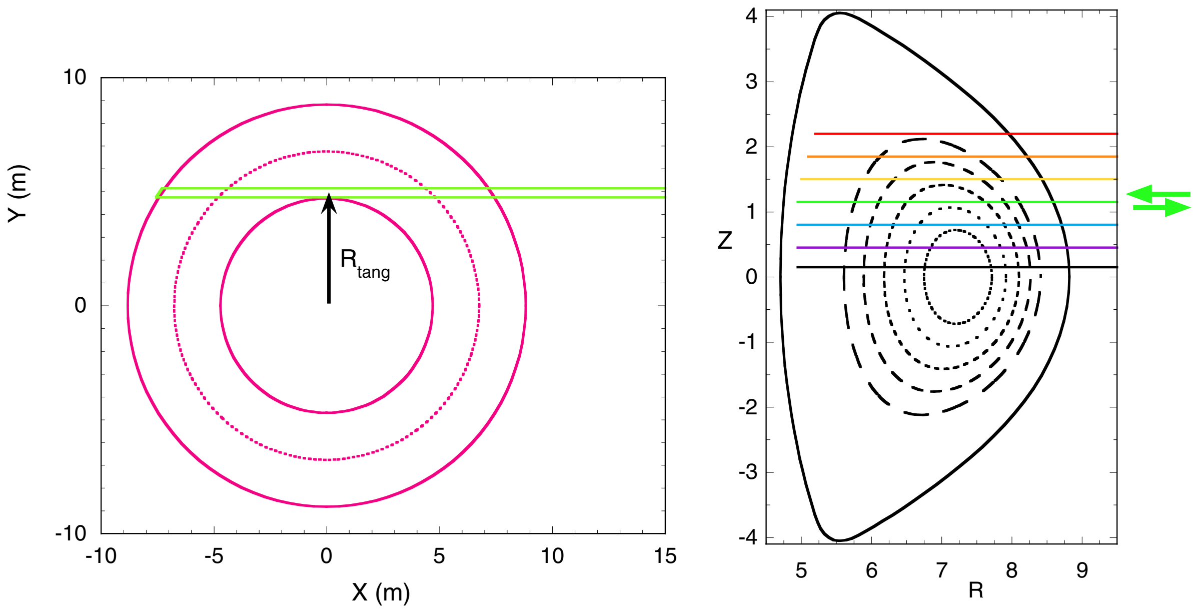

Figure 11. Plan view of tangential neutral beam injection geometry, and side view showing vertically displaced beam-axis paths.

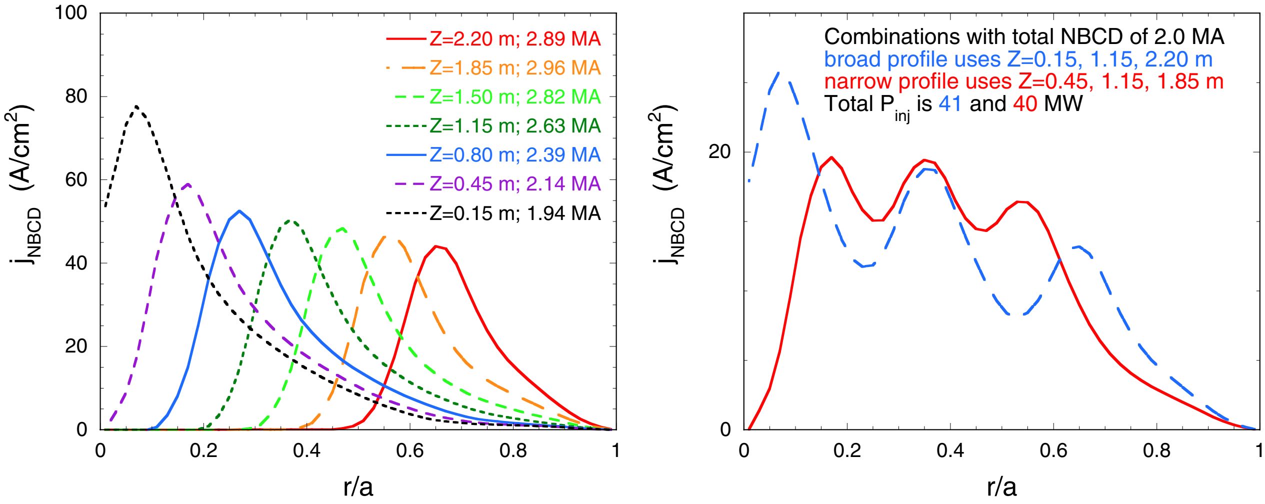

Figure 12. Left: neutral beam driven current density, labeled with beam-axis elevation and total beam-driven current for 50 MW injected. Right: neutral beam driven current density for broadly and tightly spaced combinations of three beam-axis elevations.

structure. This greatly restricts range of feasible orientations. Maximizing the current drive efficiency calls for large $v_{\|}/v$, or aiming as tangential as possible. Taken together, these constraints typically place the tangency radius (minimum major radius along the beam path) inside the plasma but not far from the inboard wall (see figure 11). This avoids large shine-through power on the inner wall, and the long path length through the plasma reduces the shine-through at the outer wall in low-density phases of operation. The density of the burning plasma phase is high enough to stop the beam mostly along the entry leg as the path approaches its minimum minor radius. This type of orientation can generally be achieved without special shaping for the outer TF coil legs, but does require tailored shaping of breeder and shield modules and the neutral beam duct.

While the toroidal location and toroidal angle of the beam path is narrowly constrained by tokamak hardware, the poloidal location and direction is not, so it will be chosen to match the desired radial range of the beam-driven current. The ITER beam design is stationary, but the extracted ion beam can be steered to vary the elevation, Z, of the beam footprint at the tangency radius over a range of 0.6 m. Calculations for the ACT2 design study [18] found that tipping the beamline out of the midplane further extended the range of possible shapes for the current profile. However, using this approach to localize the deposition for $0.4 < r/a < 0.7$ would require extreme tipping of the NB system, so we have considered a different geometry: mounting the neutral beams above or below the midplane, while maintaining a horizontal orientation for the beam axes. The vertical displacement of the beam axis determines the minimum r/a of the deposition profile, while the peak current density is not far outside this minimum r/a.

A plan view of the quasi-tangential injection geometry and a poloidal cross-sectional view of several vertically displaced

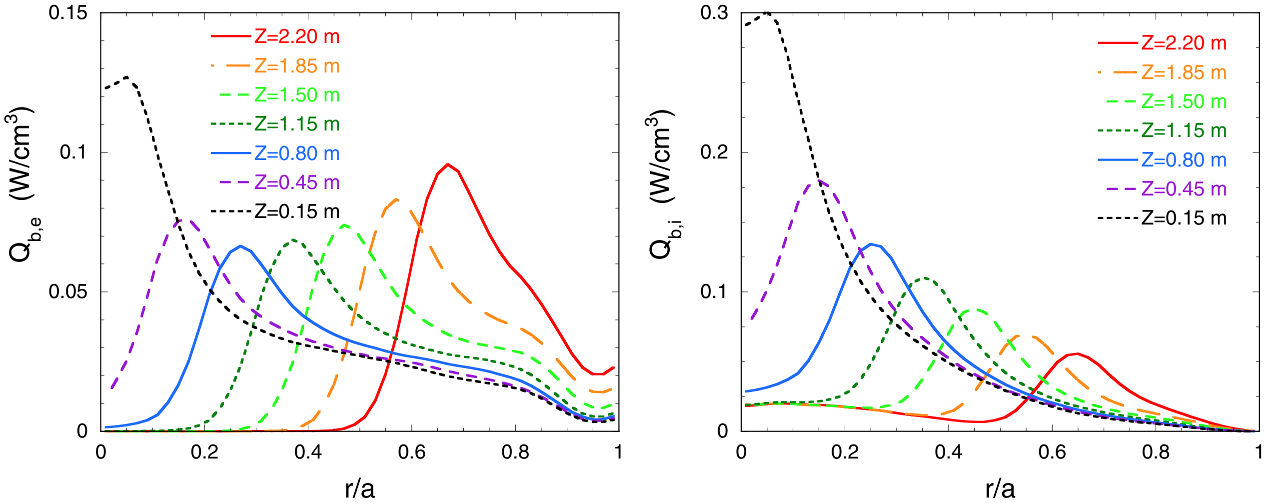

Figure 13. Neutral beam heating power density, for electrons and ions, labeled by beam-axis elevation.

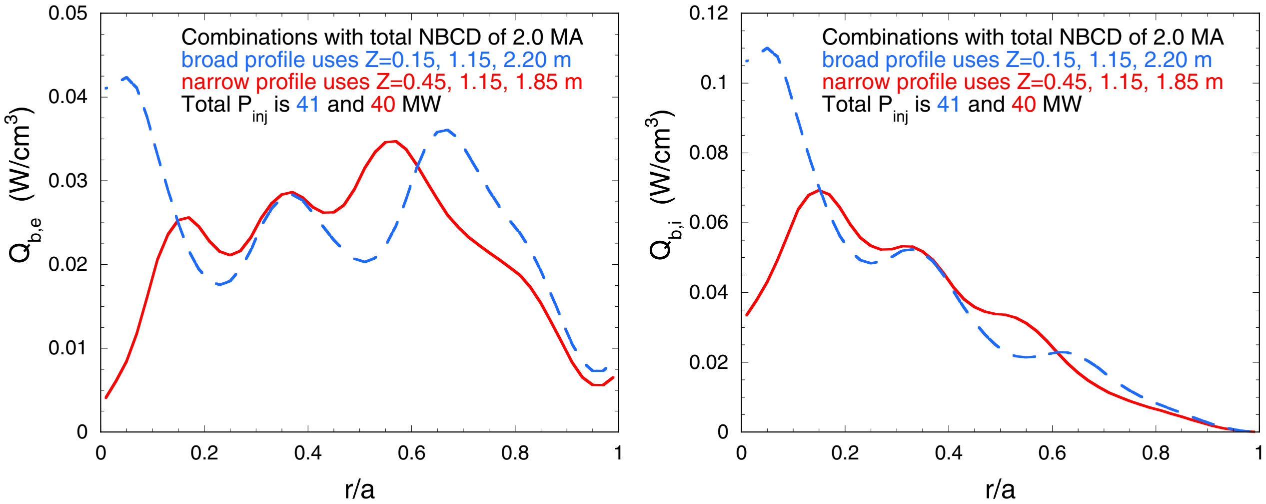

Figure 14. Neutral beam heating power density, for electrons (left) and ions (right), for broadly and tightly spaced combinations of three beam-axis elevations.

beam paths are illustrated in figure 11; these paths are used to obtain the results shown in figures 12 and 13. Filling the current drive gap between near-axis ICRH current drive and near-edge LHCD could be achieved with moderate elevation, Z, up to $\sim$2 m.

6.2. Neutral beam current drive profiles

Shown in figure 12 are a series of current density profiles for a range of beam axis displacements above the midplane from 0.15 to 2.2 m to vary the location of the local maximum in the profiles $0 < r/a < 0.6$. The total current driven by 50 MW of NB at each Z is listed in the legend.

Ion and electron heating are about equal globally, but not locally. Shown in figure 13 are a series of profiles of electron and ion heating power density, and these also exhibit a strong localization. Electron heating is dominant for large r/a (T_e is lower there so electron drag is higher), and broader than current drive with small Z. The ion heating profile has finite power at small r/a for all Z because pitch-angle scattering during thermalization causes some ions to be radially transported to the central part of the plasma. Long-distance migration of the orbit requires very substantial diffusion of the pitch-angle from its initial co-passing value and a correspondingly significant slowing down takes place during the time it takes to scatter the pitch-angle through a large angle. Low energy fast ions dominantly heat ions and their wide distribution in pitch-angle produces little net toroidal driven current, so the small r/a region of the electron heating and current drive profiles is not partially filled in by this mechanism.

The results in figure 12 correspond to current drive efficiencies of $I_{cd}R_o n_{e,20}/P_b = 0.3\text{--}0.4$ A/W m^2 or $I_{cd}/P_b = 0.04\text{--}0.06$ A W^{-1}, with the higher efficiencies occurring at larger r/a, where the density is lower. This is attractive for driving large currents, and the flexibility in radial location is also an advantage of this method. A range of beam elevations will be needed to fully fill the current drive gap between near-axis ICRH absorption and large r/a LHCD. Two simple examples are provided in figure 14, where the power of the larger $|Z|$ beams has been reduced to lower the total driven current to 2 MA, produced by 40 MW.

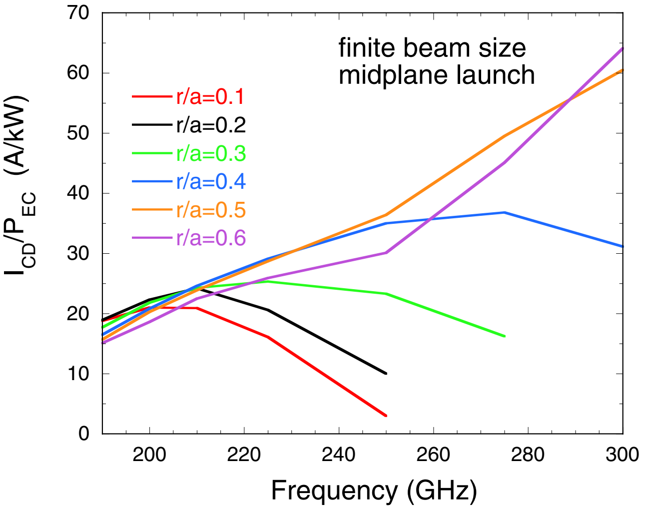

Figure 15. For midplane launchers, the maximum electron cyclotron wave current drive efficiency versus frequency, grouped by the average *r*/*a* of the driven driven current.

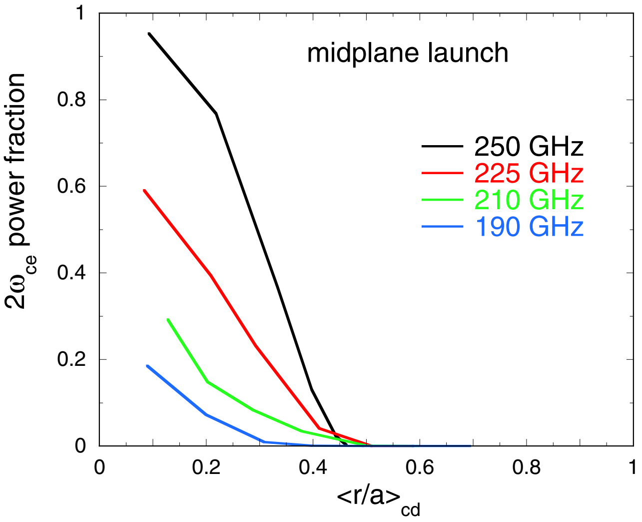

Figure 16. The power fraction absorbed by Doppler matching at the second harmonic versus the average *r*/*a* of the driven current.

7. Electron cyclotron wave heating and current drive

Electron cyclotron wave current drive is examined as a means to provide current drive in the intermediate region of the plasma, with $0.2 < r/a < 0.6$, for fine-tuning the safety factor profile and for active control of MHD instabilities. Neither conventional ICRF nor lower hybrid waves can access these intermediate radial locations. In addition, electron cyclotron waves can propagate through vacuum and therefore this technique has no plasma-coupling constraints that can affect conventional ICRF, helicon and lower hybrid waves.

The importance of the Doppler-shifted resonance between the waves and a small portion of the electron population [26] strongly complicates the parametric dependence of the wave absorption. The wave frequency, ω, and the variation of $n_{\|}$ along the path through the plasma, as well as the electron temperature all play critical roles.

For a fixed electron temperature profile, finding the optimal parameters of the ECCD components requires a four dimensional parameter scan that varies the wave frequency, launcher position, and both the poloidal and toroidal steering angles defining the direction of the launched waves. With the high temperature of the burn phase, $T_e(0) \sim 40$ keV, it is critical to minimize second harmonic absorption [36] so that power is not absorbed by a resonance with lower current drive efficiency and a broader spatial distribution. Reduced second harmonic losses have been reported for off-midplane launch [32] and 'top' launch [38], so we have examined these locations as well.

We varied the frequency between 190 and 300 GHz, while the launcher position ranged from the outer mid-plane to near the top of plasma. The range of poloidal and toroidal launch angles was tailored to each launcher position, and the occasionally strong dependence on launch angles required close spacing (1°) of the launch angles.

The O-mode polarization is launched from a location just outside the plasma on the low-field side. The condition for the waves to avoid significant refraction is $\omega_{pe}^2/\omega_{ce}^2 \ll 1$, or $10.3(n_e/10^{20}\ \mathrm{m}^{-3})/(B_o/T)^2 \ll 1$, which is easily satisfied with the frequencies studied here.

For electron cyclotron waves the standalone GENRAY ray-tracing code [37, 55] was used to calculate ray propagation, heating and current drive. Absorption is calculated using the anti-Hermitian relativistic dielectric tensor for an electron plasma. The electron velocity-space distribution is assumed to be Maxwellian. The Lin-Liu current-drive model [75] is used, which includes fully relativistic electron dynamics, momentum-conserving effects [76, 77] in electron–electron collisions, and a simplified quasilinear RF diffusion operator describes wave-particle interactions.

The results shown below do not include current drive arising from absorption at the second harmonic because this does not have the characteristics that are typically desired from an EC system: the profile shape is broad, $0.2 \leqslant r/a \leqslant 0.6$, with a peak at $r/a = 0.35-0.40$, and the profile location depends weakly on frequency and launcher position. The total current driven by second harmonic absorption can be as large as 50% of the current driven at the fundamental resonance if the latter is located at $r/a \leqslant 0.1$ and the frequency is ~225 GHz and a midplane launcher is used. Other frequencies and off-midplane launcher positions discussed below suffer less second harmonic absorption and have correspondingly less second harmonic current drive. The results shown *do* include the effect of wave power 'lost' at the second harmonic—less power is available when the waves reach the fundamental resonance—but the current drive arising from second harmonic absorption is not included in figures 15 or 18–22.

The second harmonic absorption is not significant when the electron temperature is reduced by 50% or more, so near-axis current drive becomes feasible at 225 GHz with an efficiency of 25 A kW^{-1}. With these lower temperatures, however, the current drive efficiency is reduced at 225 GHz for $r/a = 0.5$, and at all radii for lower frequencies.

Survey calculations were carried out with the single-ray model in GENRAY, but for selected cases a more complete

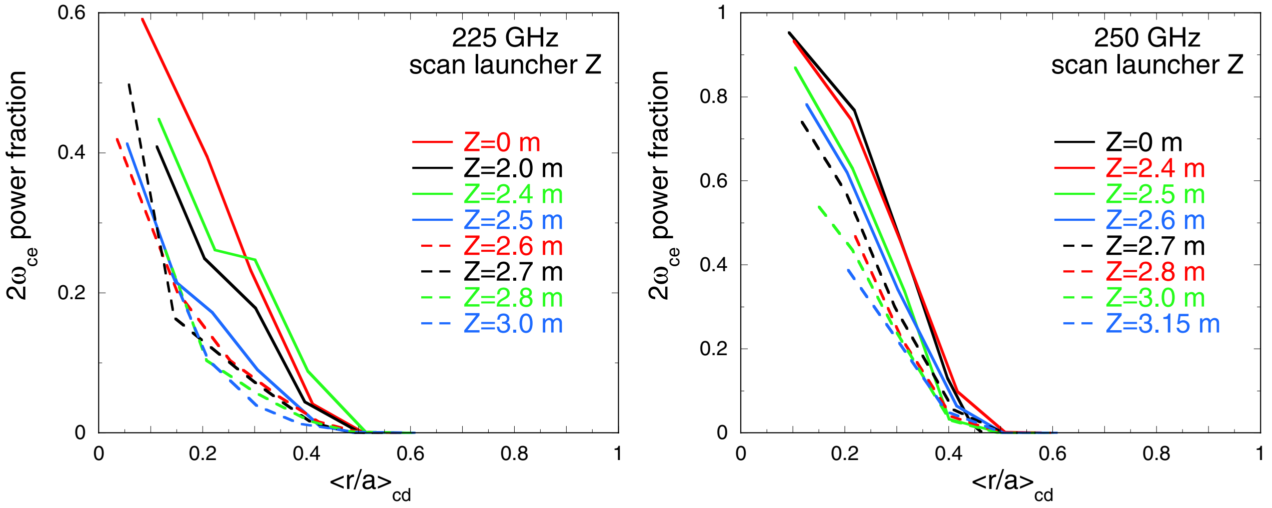

Figure 17. The power fraction absorbed by Doppler matching at the second harmonic versus the average *r*/*a* of the driven current for a scan of launcher elevation. Left: 225 GHz, right: 250 GHz.

calculation was done with GENRAY's standard finite beam size model, with 48 rays, and an assumed divergence angle of 1.2°, which is a typical minimum value caused by the finite size of the EC launcher. Strong edge turbulence may also affect the spreading of the beam [28, 78–80], but a quantitative estimate of this effect cannot be reliably predicted at this time, so this is not included. A number of additional effects can lead to broadening [28], but all of them have been ignored for this preliminary survey. In most cases the calculations with finite divergence produce a broader radial profile, but it is often still a 'localized' profile, with $\Delta r/a \sim 0.15$ (FWHM), as shown below. We note again that this degree of localization and the figures are based solely on current drive at the fundamental resonance; the second harmonic current drive is not useful for NTM control, but it might make a useful contribution to fine tuning the safety factor profile.

7.1. Electron cyclotron midplane launch

Figure 15 provides an overview of the results for *midplane* launchers, placed at $R = 8.96$ m. The highest achievable current drive efficiency is shown as a function of frequency for each of the selected radial locations. The highest overall current drive efficiency is obtained with high frequency, but the highest efficiencies are possible only for current drive located at $r/a \geqslant 0.5$. Absorption near the magnetic axis at these frequencies requires higher $n_{\|}$, and this leads to strong second harmonic absorption at mid-radius, leaving little or no power to drive current near the axis. The $2\Omega_{ce}$ absorption is quite strongly dependent on current drive location as shown in figure 16, with this loss channel growing rapidly as *r*/*a* diminishes or frequency rises. Second harmonic absorption is not a significant problem for frequencies up to ~210 GHz; so all locations are accessible with similar efficiency, but it is uniformly lower than at higher frequencies: only 15–25 A kW^{-1} (figure 15).

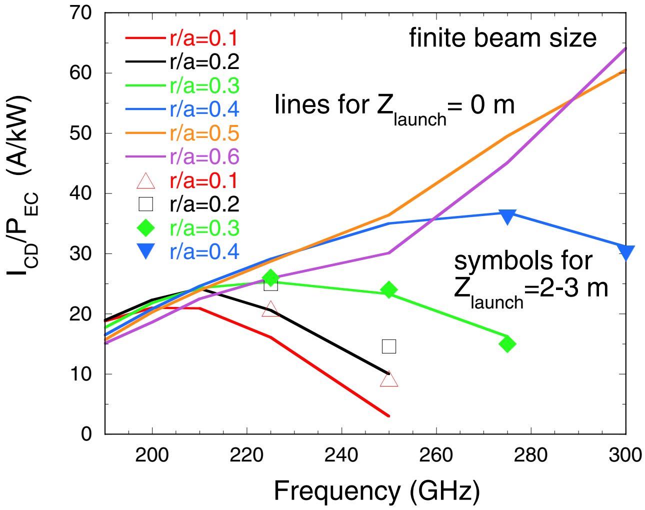

Figure 18. Electron cyclotron wave current drive efficiency versus frequency. grouped by the average *r*/*a* of the driven driven current. Lines denote midplane launchers, isolated symbols represent off-midplane launchers.

7.2. Electron cyclotron off-midplane launch

Launching from a position with large *Z* and smaller *R* serves to reduce $2\Omega_{ce}$ absorption, by avoiding the outboard part of the plasma where the local second harmonic is closer to the wave's frequency and resonance is more easily achieved (see figure 17). By this means, access to smaller radii, $r/a > 0.2$, with reasonable current drive efficiency becomes achievable at 225 GHz. For 250 GHz, however, even high Z_{launch} has large $2\Omega_{ce}$ absorption and the improvement is smaller for even higher frequencies. Most of the reduction in $2\Omega_{ce}$ absorption is obtainable without requiring 'top' launch at the maximum *Z* of the boundary, where access is much more difficult.

In spite of the reduced second harmonic absorption, launcher positions out of the midplane do not actually provide much improvement when finite-size beams of EC radiation

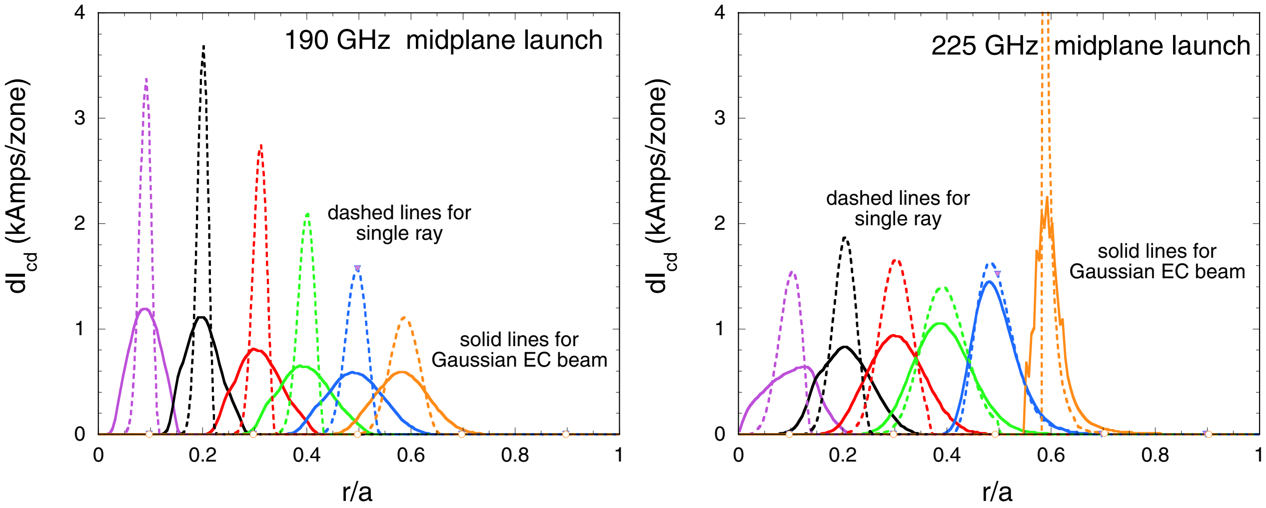

Figure 19. Comparison of electron cyclotron wave current drive profiles as calculated by GENRAY's single-ray model and the multi-ray finite-beam-size model, for midplane launcher at 190 (left) and 225 (right) GHz. The plotted quantity is the driven current per radial zone, to total driven current is proportional to the area under each curve.

are modeled (figure 18). A similar figure based on single-ray calculations does show modest improvement, but this is not present in the more comprehensive calculations with finite size beams because the collection of ray paths leading to high efficiency near the axis have a very narrow range of directions that cannot fully include even a beam with divergence of only ~1°.

Although high Z_{launch} improves current drive efficiency near the magnetic axis relative to the value obtained with midplane launch *at the same frequency*, for any given target *r*/*a* the current drive efficiency is only marginally greater than what can be obtained from a midplane launch at *lower* frequencies. For instance, at $r/a = 0.2$ midplane launch at 210 GHz is almost as efficient as 225 GHz with $Z_{\mathrm{launch}} = 2.6$ m. While the current drive efficiency at all radii is low with 190 GHz, this frequency is closer to currently available technology, and it can drive significant current over a very broad range of *r*/*a*.

Although at 225 and 250 GHz the current drive efficiency for $r/a \leqslant 0.2$ is improved relative to the same frequency launched from the midplane, this improvement is not obtainable for even higher frequencies because they are too close to the local second harmonic frequency to avoid strong second harmonic absorption when attempting to drive current near the magnetic axis.

Significant drawbacks of high Z_{launch} are that access is more limited than near the midplane, and that changes in the Shafranov shift can strongly affect the accessible range of *r*/*a*.

7.3. Electron cyclotron single-ray versus multi-ray model

For midplane launchers the frequently used single-ray approximation frequently *does* yield reliable estimates of both the *r*/*a* average of the driven current and the current drive efficiency. However, it tends to seriously underestimate the width of the current drive profile (see figure 19), so when this is important a finite size EC beam model should be used. This is of critical importance when assessing the utility of ECCD for controlling MHD activity such as neoclassical tearing modes [27–29].

The results shown here are based on a divergence of 1.2°, but this should be considered a generic minimum divergence, typical of diffraction caused by finite mirror size. Additional sources of beam broadening are discussed just before the beginning of section 7.1. With the finite beam size model the radial width of the current drive profile is $\Delta r/a \sim 0.15$ (FWHM) for midplane launchers and frequencies up to 225 GHz. A broader divergence would reduce the usefulness of ECCD for NTM control, and would strengthen our conclusion that off-midplane launchers are not capable of driving localized current near the magnetic axis

To improve readability, the quantity plotted in figures 19–22 is the driven current, $\mathrm{d}I_{\mathrm{cd}} = j_{\mathrm{tor}}\mathrm{d}A$, in each of GENRAY's 200 radial zones (`s_cur_den_toroidal*binarea` from the `netcdf` output file). The toroidal current density becomes very large when the target location is near the magnetic axis (especially in single-ray calculations) so the driven current profiles are rather close to the radial axis when they are located at $r/a \geqslant 0.5$. The peaks of the $\mathrm{d}I_{\mathrm{cd}}$ profiles, however, are much more comparable in a scan over target *r*/*a*, so the details can be more easily grasped.

The single-ray and finite-size models also agree for high frequencies launched at the midplane (figure 20), but here both models produce broad deposition profiles. The cause of the broadening is that with mid-plane launch, the Doppler resonance is far out on the Maxwellian tail for 250 GHz and higher, so absorption is weaker and spread over a longer section of the beam path, which translates into a radially extended deposition which is larger than the finite size of the beam as projected onto the radial direction. At 275 and 300 GHz the radial width of the current drive profile is much larger: $\Delta r/a = 0.4$ at $r/a = 0.5$.

With high Z_{launch}, however, the Doppler resonance is not as far out on the Maxwellian tail as it is for midplane launch at the same frequency, so the absorption is stronger and a

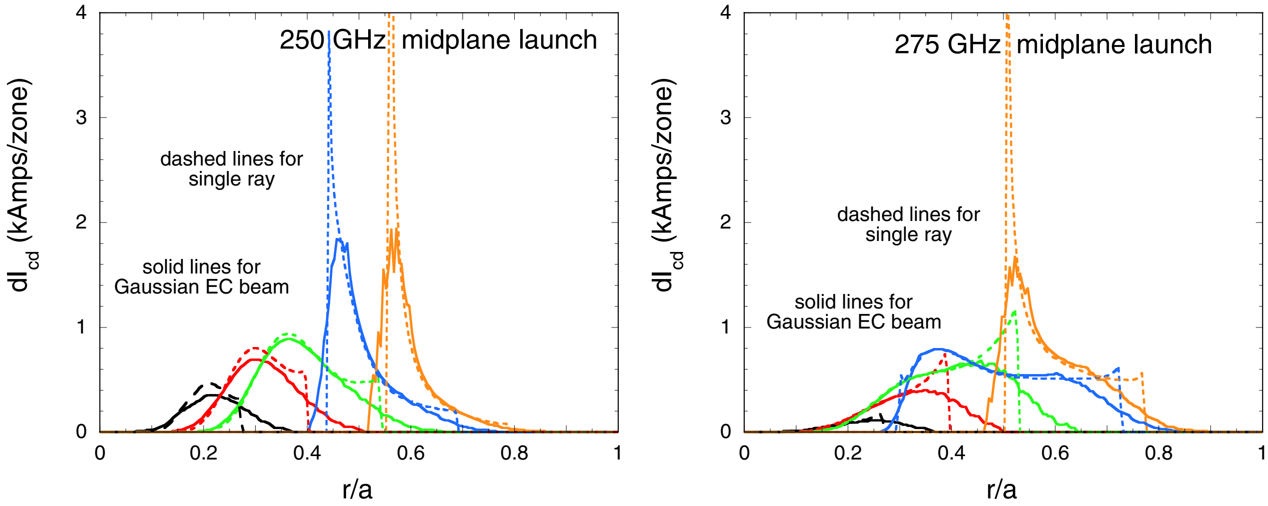

Figure 20. Comparison of electron cyclotron wave current drive profiles as calculated by GENRAY’s single-ray model and the multi-ray finite-beam-size model, for midplane launcher at 250 and 275 GHz.

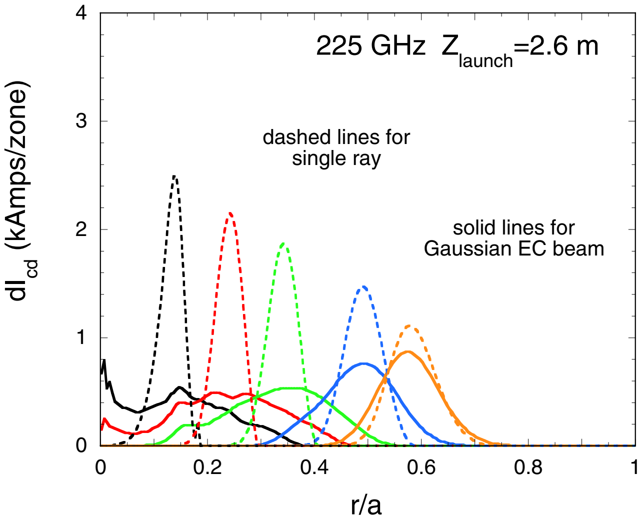

Figure 21. Comparison of electron cyclotron wave current drive profiles as calculated by GENRAY’s single-ray model and the multi-ray finite-beam-size model, for $Z = 2.6$ m launcher at 225 GHz.

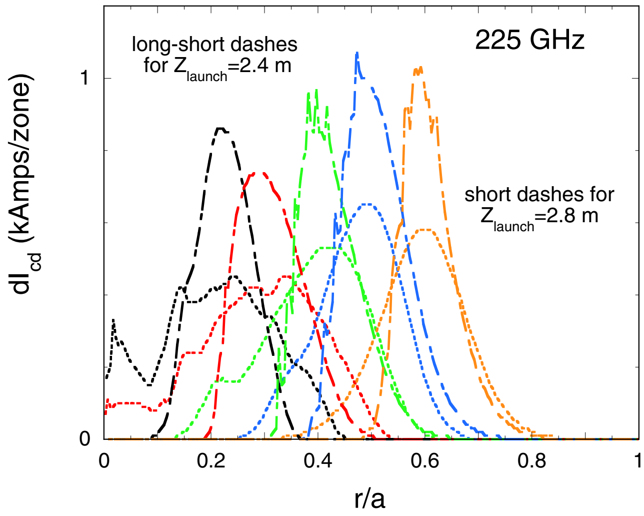

Figure 22. Comparison of electron cyclotron wave current drive profiles as calculated by GENRAY’s multi-ray finite-beam-size model, for $Z = 2.4$ and 2.8 m launchers at 225 GHz.

single ray calculation produces an unrealistically narrow current profile that is narrower than that calculated for a finite beam width, as shown in figure 21. Here the radial width of the current drive profile is larger than with midplane launch at 225 GHz (or lower): $\Delta r/a \geqslant 0.25$ (FWHM) for $r/a < 0.4$.

With very high Z_{launch} (see figure 22), the radial location of the deposition depends very sensitively on the steering angles, so the different parts of a finite size EC beam lead to deposition over a broader radial range than seen with less extreme off-midplane launchers. The higher peak current density with moderate off-midplane Z_{launch} is more useful for MHD control.

In summary, the highest EC current drive efficiency is achieved with 275–300 GHz, but is limited to $r/a \geqslant 0.5$. High efficiency at $r/a \sim 0.4$ is possible with 250 GHz, but driving current closer to the magnetic axis requires lower frequencies and correspondingly lower efficiencies. The frequency range 190–210 GHz, launched from the outer midplane provides the greatest flexibility in current drive location, reaching normalized minor radius of 0.1–0.6, but with current drive efficiency of only 15–25 A kW^{-1} (varying with frequency, not r/a). Although providing bulk plasma current with EC is impractical with these low efficiencies, its flexibility in deposition location can be useful for controlling the safety factor profile and stabilizing neoclassical tearing modes [28, 29].

8. Summary and discussion

Heating and current drive performance is calculated for five types of system, based on the burning plasma operating conditions of the K-DEMO tokamak. The results provide a detailed guide for optimizing current drive efficiency, identifying the system parameters needed to drive current at different minor radii. A combination of systems will probably be needed to efficiently drive the current profile needed to optimize the MHD stability.

Lower hybrid waves at 5 GHz can drive current in the outer third of the plasma minor radius, with an efficiency of 30–45 A kW^{-1}, depending on the poloidal location of the launcher and the launched $n_{\|}$. The driven current density profile shape can be varied considerably within this radial range by changing the launched $n_{\|}$.

With a midplane launcher, ion cyclotron fast waves at 74–80 MHz (chosen to minimize alpha damping), can drive current near the magnetic axis ($r/a < 0.3$) with an efficiency of 60–70 kA/MW. Varying the frequency within this range has a small effect on the driven current, but the bulk ion heating varies from 30–15%.

Helicon fast wave performance was surveyed by varying frequency over 0.6–2.5 GHz, launcher position from top to bottom on the low field side, and launched $n_{\|}$ from -1.6 to -3. We have assumed there are no losses in the SOL: that all of the launched power propagates as a fast wave to the last closed flux surface. With frequencies of 1–2.5 GHz, current drive efficiency of 55–70 kA/MW is obtainable; the range of possible launcher positions expands as the frequency rises. The current drive efficiency and location of the current drive depends weakly on the frequency and launcher location, so it is possible to choose a launcher location that will be acceptable for a range of frequencies and $n_{\|}$. Unfortunately, the radial location, $r/a \sim 0.6$, of the current drive is quite insensitive to the choice of frequency, launcher position and $n_{\|}$; it is essentially fixed by the temperature profile and the equilibrium.

Two technologies, neutral injection and electron cyclotron waves, have considerable flexibility in driving current throughout the radial range between central IC and edge LH. Beam steering allows great flexibility in targeting r/a as long as the beam port is tall enough to accommodate paths that are out of the midplane; a beam axis vertically displaced by 2 m from midplane will place the driven current peak at $r/a = 0.6$. Choice of EC frequency and launcher geometry (including toroidal and poloidal steering of the launched waves) provide control over the wave absorption location.

Neutral beam injection based on ITER 1 MeV design parameters can drive current for any $r/a \leqslant 0.7$ with a current drive efficiency of 40–60 A kW^{-1} (lowest near the magnetic axis).

Electron cyclotron waves at 190–210 GHz can drive localized current for any $r/a \leqslant 0.7$ with a current drive efficiency of 20–25 A kW^{-1}. Higher current drive efficiencies are possible at larger minor radius ($r/a \geqslant 0.3$) and larger frequency. The highest current drive efficiencies, 50–60 A kW^{-1}, are only possible near mid-radius, $0.5 \leqslant r/a \leqslant 0.6$, with 275–300 GHz, but these current drive profiles are much broader than seen with frequencies $\leqslant$250 GHz. Midplane launch is suitable for high current drive efficiency, even though second harmonic absorption can limit performance at higher frequencies. We find that when a minimal level of finite beam divergence is accounted for (1.2°) the use of high-Z launchers does not produce better results than can be obtained by using a lower frequency with a midplane launcher.

Lower hybrid and electron cyclotron waves heat only electrons. When IC systems are optimized for current drive and to minimize alpha particle absorption, the ion heating fraction is 15–30%.. A similarly optimized helicon wave system will have negligible ion heating. An IC or helicon wave system can be used for stronger ion heating, but it will be a less efficient current driver in that case. Globally, neutral beam injection produces roughly equal electron and ion heating, but the radial profile shapes differ: electron heating is stretched toward the edge, while ion heating is enhanced at smaller minor radii. Consequently, local ratios of ion to electron heating vary considerably and the heating profiles are not as localized as the driven current profiles.

Future LH and IC studies could include ‘inside’ launcher locations along the small major radius side of the vacuum vessel wall, because that region offers some advantages [11, 12] that may offset the difficulty of access.

Acknowledgments

We thank R. Prater, A. Garofalo and J.C. Wright for enlightening discussions. This research was supported by the National Fusion Research Institute, Daejeon, the Republic of Korea, under a research agreement with Princeton University, and by the U.S. Department of Energy under Contract No. DE-AC02-09CH11466 with Princeton University. Use of the research computer clusters at PPPL is gratefully acknowledged.

Notice: This manuscript is based upon work supported by the U.S. Department of Energy, Office of Science, Office of Fusion Energy Sciences, and has been authored by Princeton University under Contract Number DE-AC02-09CH11466 with the U.S. Department of Energy. The publisher, by accepting the article for publication acknowledges, that the United States Government retains a non-exclusive, paid-up, irrevocable, world-wide license to publish or reproduce the published form of this manuscript, or allow others to do so, for United States Government purposes.

ORCID iDs

D.R. Mikkelsen https://orcid.org/0000-0003-0865-3703
C.E. Kessel https://orcid.org/0000-0002-2072-1134
F.M. Poli https://orcid.org/0000-0003-3959-4371

References

[1] Kim K. *et al* 2015 *Nucl. Fusion* **55** 053027
[2] Hemsworth R. *et al* 2009 *Nucl. Fusion* **49** 045006
[3] Messiaen A., Koch R., Weynants R., Dumortier P., Louche F., Maggiora R. and Milanesio D. 2010 *Nucl. Fusion* **50** 025026
[4] Henderson M. *et al* 2015 *Phys. Plasmas* **22** 021808
[5] Bibet P., Litaudon X. and Moreau D. 1995 *Nucl. Fusion* **35** 1213
[6] Becoulet A. *et al* 2011 *Fusion Eng. Des.* **86** 490–96 (*Proc. of the 26th Symp. of Fusion Technology*)
[7] Ogawa T. *et al* 2001 *Nucl. Fusion* **41** 1767

[8] Wang S.J., Wi H.H., Kim H.J., Jeong J.H. and Kwak J.G. 2016 Measurement and analysis of helicon wave couplings for current drive in KSTAR *43rd EPS Conf. on Plasma Physics (Leuven, 4–8 July 2016)* Poster P4.038 (http://ocs.ciemat.es/EPS2016PAP/html/)

[9] Prater R., Moeller C., Pinsker R., Porkolab M., Meneghini O. and Vdovin V. 2014 *Nucl. Fusion* **54** 083024

[10] Pinsker R.I. 2015 *Phys. Plasmas* **22** 090901

[11] Wallace G.M. *et al* 2015 *AIP Conf. Proc.* **1689** 030017 (http://aip.scitation.org/doi/pdf/10.1063/1.4936482)

[12] Wallace G.M. *et al* 2016 *IEEE Trans. Plasma Sci.* **44** 1613–8

[13] Hannan A., Hellsten T. and Johnson T. 2013 *Nucl. Fusion* **53** 043005

[14] Lerche E., Van Eestera D., Messiaen A., Franke T. and EFDA-PPPT Contributors 2014 *AIP Conf. Proc.* **1580** 338–41

[15] Brambilla M. and Bilato R. 2015 *Nucl. Fusion* **55** 023016

[16] Kazakov Y.O., Eester D.V., Wauters T., Lerche E. and Ongena J. 2015 *Plasma Phys. Control. Fusion* **57** 025014

[17] Kessel C.E., Poli F.M., Ghantous K., Gorelenkov N.N., Rensink M.E., Rognlien T.D., Snyder P.B., John H.S. and Turnbull A.D. 2015 *Fusion Sci. Technol.* **67** 75–106

[18] Kessel C.E. and Poli F.M. 2015 *Fusion Sci. Technol.* **67** 220–39

[19] Chiu S., Chan V., Harvey R. and Porkolab M. 1989 *Nucl. Fusion* **29** 2175

[20] Koch R., Lerche E., Van Eester D. and Nightingale M. 2011 *AIP Conf. Proc.* **1406** 349–52

[21] Vdovin V.L. 2013 *Plasma Phys. Rep.* **39** 95–119

[22] Pinsker R.I. 1994 *AIP Conf. Proc.* **289** 179–91

[23] Pinsker R., Moeller C., deGrassie J., Petty C., Anderson J., Torreblanca H., Porkolab M., Lau C., Watkins J. and Zeng L. 2016 *Bull. Am. Phys. Soc.* **61** 66

[24] Wang S., Wi H., Kim H., Kim J., Jeong J. and Kwak J. 2017 *Nucl. Fusion* **57** 046010

[25] Wang S.J., Kim J., Jeong J.H., Kim H.J., Joung M., Bae Y.S. and Kwak J.G. 2015 *AIP Conf. Proc.* **1689** 030014

[26] Prater R. 2004 *Phys. Plasmas* **11** 2349–76

[27] Bertelli N., Lazzari D.D. and Westerhof E. 2011 *Nucl. Fusion* **51** 103007

[28] Poli E. *et al* 2015 *Nucl. Fusion* **55** 013023

[29] Figini L., Farina D., Henderson M., Mariani A., Poli E. and Saibene G. 2015 *Plasma Phys. Control. Fusion* **57** 054015

[30] Poli F., Fredrickson E., Henderson M., Kim S.H., Bertelli N., Poli E., Farina D. and Figini L. 2018 *Nucl. Fusion* **58** 016007

[31] Farina D., Henderson M., Figini L., Ramponi G. and Saibene G. 2012 *Nucl. Fusion* **52** 033005

[32] Poli E., Tardini G., Zohm H., Fable E., Farina D., Figini L., Marushchenko N. and Porte L. 2013 *Nucl. Fusion* **53** 013011

[33] Farina D., Henderson M., Figini L. and Saibene G. 2014 *Phys. Plasmas* **21** 061504

[34] Takahashi K., Kajiwara K., Oda Y., Sakamoto K., Omori T. and Henderson M. 2015 *Fusion Sci. Technol.* **67** 718–31

[35] Wenninger R. *et al* 2015 *Nucl. Fusion* **55** 063003

[36] Smith G.R., Cohen R.H. and Mau T.K. 1987 *Phys. Fluids* **30** 3633–5

[37] Harvey R. and McCoy M. 1993 *Proc. IAEA Technical Committee on Advances in Simulation and Modeling of Thermonuclear Plasmas (Montreal, 15–18 June 1992)* (Vienna: IAEA) p 489 USDOC NTIS Doc. No. DE93002962

[38] Garofalo A. 2014 *Nucl. Fusion* **54** 073015

[39] Kessel C., Kim K., Yeom J.H., Brown T., Titus P. and Neilson G. 2013 Systems analysis exploration of operating points for the Korean demo program *IEEE 25th Symp. on Fusion Engineering (San Francisco, 10–14 June 2013)* (http://ieeexplore.ieee.org/xpl/mostRecentIssue.jsp?punumber=6624144)

[40] Dragojlovic Z., Raffray A.R., Najmabadi F., Kessel C., Waganer L., El-Guebaly L. and Bromberg L. 2010 *Fusion Eng. Des.* **85** 243–65

[41] Jardin S.C. *et al* 1993 *Nucl. Fusion* **33** 371

[42] Tang W. 1986 *Nucl. Fusion* **26** 1605

[43] Kessel C. *et al* 2007 *Nucl. Fusion* **47** 1274

[44] Angioni C., Fable E., Greenwald M., Maslov M., Peeters A.G., Takenaga H. and Weisen H. 2009 *Plasma Phys. Control. Fusion* **51** 124017

[45] Angioni C., McDermott R., Fable E., Fischer R., Pütterich T., Ryter F., Tardini G. and The ASDEX Upgrade Team 2011 *Nucl. Fusion* **51** 023006

[46] Snyder P., Groebner R., Hughes J., Osborne T., Beurskens M., Leonard A., Wilson H. and Xu X. 2011 *Nucl. Fusion* **51** 103016

[47] Fisch N.J. and Boozer A.H. 1980 *Phys. Rev. Lett.* **45** 720–2

[48] Bonoli P.T. and Englade R.C. 1986 *Phys. Fluids* **29** 2937–50

[49] Imbeaux F., Peysson Y. and Eriksson L.G. 2003 *AIP Conf. Proc.* **694** 271–4

[50] Barbato E. and Santini F. 1991 *Nucl. Fusion* **31** 673

[51] Spada M., Bornatici M. and Engelmann F. 1991 *Nucl. Fusion* **31** 447

[52] Wang J., Zhang X., Yu L. and Zhao X. 2014 *AIP Conf. Proc.* **1580** 458–61 (http://aip.scitation.org/doi/pdf/10.1063/1.4864587)

[53] Belo J.H. *et al* 2011 *Nucl. Fusion* **51** 083017

[54] Ignat D., Valeo E. and Jardin S. 1994 *Nucl. Fusion* **34** 837

[55] Smirnov A. *et al* 2009 *Proc. of the 15th Workshop on ECE and ECRH (Yosemite, 10–13 March 2008)* (Singapore: World Scientific) p 301 (http://worldscientific.com/worldscibooks/10.1142/6859#t=toc)

[56] Bonoli P. *et al* 2006 *Plasma Physics and Controlled Nuclear Fusion Research: Proc. 21st Int. Conf. on Fusion Energy (Chengdu, 16–21 October 2006)* (Vienna: IAEA) CD–ROM file PD–3 (http://naweb.iaea.org/napc/physics/FEC/FEC2006/html/node74.htm#19381)

[57] Brambilla M. 1978 *Nucl. Fusion* **18** 493

[58] Hawryluk R.J. 1980 *Physics of Plasmas Close to Thermonuclear Conditions: Proc. Course (Varenna, 27 August–8 September 1979) vol* 1 (Brussels: Commision of the European Communities) pp 19–46 (https://sciencedirect.com/science/book/9781483283852)

[59] Goldston R.J. 1986 *Basic Physical Processes of Toroidal Fusion Plasmas: Proc. Course and Workshop (Varenna, 26 August–3 September 1985) vol* 1 (Perugia: Monotypia Franchi) pp 165–86

[60] Brambilla M. 1999 *Plasma Phys. Control. Fusion* **41** 1

[61] Wright J.C., Bonoli P.T., Brambilla M., Meo F., D'Azevedo E., Batchelor D.B., Jaeger E.F., Berry L.A., Phillips C.K. and Pletzer A. 2004 *Phys. Plasmas* **11** 2473–9

[62] Bertelli N., Valeo E., Green D., Gorelenkova M., Phillips C., Podest M., Lee J., Wright J. and Jaeger E. 2017 *Nucl. Fusion* **57** 056035

[63] Ehst D. and Karney C. 1991 *Nucl. Fusion* **31** 1933

[64] Wright J., Phillips C. and Bonoli P. 1997 *Nucl. Fusion* **37** 1349

[65] Bilato R., Brambilla M., Pavlenko I. and Meo F. 2002 *Nucl. Fusion* **42** 1085

[66] Lau C., Jaeger E.F., Bertelli N., Berry L.A., Blazevski D., Green D.L., Murakami M., Park J.M., Pinsker R.I. and Prater R. 2015 *AIP Conf. Proc.* **1689** 080011

[67] Lau C., Jaeger E., Bertelli N., Berry L., Green D., Murakami M., Park J., Pinsker R. and Prater R. 2017 AORSA full wave calculations of helicon waves in DIII-D and ITER *Nucl. Fusion* submitted

[68] Jaeger E.F., Berry L.A., D'Azevedo E., Batchelor D.B. and Carter M.D. 2001 *Phys. Plasmas* **8** 1573–83
[69] Bertelli N. *et al* 2016 *Nucl. Fusion* **56** 016019
[70] Bertelli N. *et al* 2015 *AIP Conf. Proc.* **1689** 030010
[71] Jardin S., Kessel C., Bathke C., Ehst D., Mau T., Najmabadi F. and Petrie T. 1997 *Fusion Eng. Des.* **38** 27–57
[72] Jardin S. *et al* 2006 *Fusion Eng. Des.* **80** 25–62
[73] Pankin A., McCune D., Andre R., Bateman G. and Kritz A. 2004 *Comput. Phys. Commun.* **159** 157–84
[74] Hemsworth I.R. 2014 private communication
[75] Lin-Liu Y.R., Chan V.S. and Prater R. 2003 *Phys. Plasmas* **10** 4064–71
[76] Prater R. *et al* and The ITPA Steady State Operation Topical Group 2008 *Nucl. Fusion* **48** 035006
[77] Marushchenko N.B., Beidler C.D., Kasilov S.V., Kernbichler W., Maassberg H., Prater R. and Harvey R.W. 2011 *Phys. Plasmas* **18** 032501
[78] Casson F., Poli E., Angioni C., Buchholz R. and Peeters A. 2015 *Nucl. Fusion* **55** 012002
[79] Sysoeva E., da Silva F., Gusakov E., Heuraux S. and Popov A. 2015 *Nucl. Fusion* **55** 033016
[80] Snicker A., Poli E., Maj O., Guidi L., Khn A., Weber H., Conway G., Henderson M. and Saibene G. 2018 *Nucl. Fusion* **58** 016002